

Experimental and numerical investigation of LOX/Methane Cryogenic Combustion at low mixture ratio

M. Théron ^{1*}, M. Martin Benito¹, B. Vieille¹, L. Vingert ², N. Fdida ², Y. Mauriot ² and R. Blouquin³, C.Seitan³, M. Onori³, L. Lequette³

¹CNES – Launcher Directorate, 52 rue Jacques Hillairet, 75012, Paris, France

²ONERA – The French Aerospace Lab, 91761, Palaiseau, France

³CT Ingénierie Paris (CTI), Imm. Arago I, 41 Bd Vauban, 78280 Guyancourt, France

*corresponding author : marie.theron@cnes.fr

Abstract

CNES ONERA and CTI are contributing to the preparation of next reusable launchers LOX/CH₄ engines through research activities studying the characterization of cryogenic LOX/CH₄ combustion in rocket engine gas generators conditions, at low mixture ratio and with both propellants injected in transcritical / liquid conditions. Several reactive coaxial mono-injector test-cases including flame visualizations have been built at ONERA MASCOTTE test bench, all characterized by measured hot gas temperatures lower than theoretical chemical equilibrium temperature. Numerical simulations are ongoing to study possible causes for temperature deficit, using a reduced kinetic scheme adapted to low mixture ratio methane combustion.

1. Introduction

In the frame of ESA Future Launchers Preparatory Program, a new generation of engines propelled by liquid oxygen (LOX) and methane (CH₄) for reusable launchers is being developed. The use of LOX/CH₄ in future combustion devices brings new scientific challenges for European Liquid Propulsion R&D programs. Part of these challenges are tackled within CNES Launchers Directorate R&D program, in collaboration with ONERA, through experimental investigations held at MASCOTTE test bench (cf. [1]), and through numerical simulations (RANS) performed with CPS-C code together with CT Ingénierie Paris. The present work aims at characterizing and understanding the behaviour of LOX/CH₄ cryogenic flames at very low mixture ratio (MR < 0.3), typical of LOX/CH₄ gas generators operating conditions. Such injection conditions are very specific and quite far from usual injection conditions encountered in other industrial applications using methane: both LOX and CH₄ propellants are injected in either transcritical or liquid thermodynamic state (LCH₄), and mixture ratio is so low that it is out of usual range of validity of reference kinetic schemes extensively used in LES or RANS simulations of air or LOX/CH₄ combustion.

The experimental study, carried out on the MASCOTTE test-bench of ONERA, aims at showing the peculiarities of cryogenic LOX/LCH₄ combustion at very low mixture ratio in a mono-injector coaxial configuration. Two optical diagnostics were implemented simultaneously and synchronized: the jet flame is visualized by high speed OH* chemiluminescence, and LOX and CH₄ dense gases or liquid jets are visualized by high-speed shadowgraphy. In addition, a rake of thermocouples has been installed downstream of the flame to measure hot gases temperature at different radial positions in a single plane. Four different operating points have been characterized, ranging from 25 to 55 bars, as well as two configurations of coaxial injectors: one with recess and one without recess, to enable comparison of recent test results to past test campaigns results obtained in similar range of operating conditions (cf. [2]). These past tests had revealed a particular topology for the LOX/LCH₄ flame, featuring a “double flame front” characterized by two concentric conical regions of OH* emission, one spreading close to the liquid oxygen boundary and the other located further away from the axis near the liquid methane boundary, with a larger expansion angle.

A common observation for all tested operating conditions in our recent campaign concerns the measured hot gases temperatures, sensibly lower than the theoretical chemical equilibrium temperature at injections conditions considered. This reduction of combustion efficiency for decreasing mixture ratio values is not new (cf. [3], [4], [6]) but extremely low mixture ratio LOX/CH₄ flames have not been widely studied in literature, neither experimentally nor numerically. The cause(s) for hot gases temperature loss compared to chemical equilibrium temperature has (have) not been fully demonstrated yet.

Numerical test-cases derived from recent MASCOTTE tests have been defined and are currently used to evaluate and validate RANS simulations performed using CPS-C code developed by CT Ingénierie. A reduced 9 species – 21

reactions kinetic scheme adapted to very low mixture ratio LOX/LCH₄ combustion has been preliminarily defined and compared to Gri-Mech 3.0 complete mechanism and to a semi-detailed mechanism developed by Zhukov for high pressure methane oxy-combustion (cf. [5]). Preliminary validation calculations on older MASCOTTE LOX/CH₄ test-cases (cf. G2 and T1 flames from [2]), first with transcritical LOX /gaseous CH₄, then with both transcritical LOX and CH₄, have also been performed with CPS-C using the same reduced kinetic mechanism.

2. Experimental setup

2.1 MASCOTTE High Pressure Chamber (BHP)

For this experimental test campaign, the BHP combustion chamber was used on the MASCOTTE test bench, located at ONERA Palaiseau center. The combustion chamber set-up schematic is shown on Figure 1. The BHP is a mono-injector modular chamber, already used in past studies, including 8 modules in axial direction with a 50*50mm section [2]. The BHP has modular lateral optical accesses, allowing the visualization of dense LOX and CH₄ jets and flames directly from the injector exit or in downstream sections, by changing the optical test section position in the axial direction relative to the injection plane. In this study, as flames are relatively short in axial direction, the optical module has been used only in the first axial position enabling visualization directly from the injector exit.

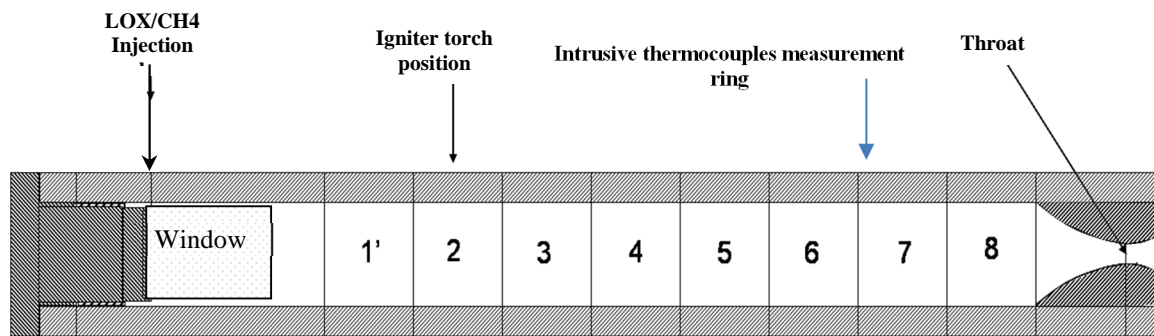


Figure 1: BHP combustion chamber set-up schematic

The injection head was fed with liquid or transcritical methane and liquid or transcritical oxygen through a single coaxial injector. The injector is a classical liquid rocket engine coaxial injector made with a central tube fed with oxygen (LOX post) and a coaxial outer tube fed with methane (cf. figure 2). Two versions of the injector have been tested, one with recess of the LOX post and one without for comparison to previous studies [2]. The injection plane is visible through the lateral optical access. It is a flat plane, i.e. the methane sleeve is not anymore protruding in the chamber as in previous campaigns (cf. [2]). Ignition of the LOX/CH₄ jets is ensured by a H₂/O₂ torch igniter positioned on the upper wall of the BHP chamber second module.



Figure 2 : Coaxial injector elements and assembly

Target chamber pressure for all operating points is ensured by using different throat diameters. During this test campaign, 2 throat diameters have been used, depending on target operating points.

2.2 Operating conditions

For the injector including a recess, 4 operating conditions have been characterized, each with several repetitions, showing a good reproducibility of operating conditions. Thus, in the following paragraphs, only 4 representative tests, one for each operating point, are analysed.

Two operating points : LL and LH, have subcritical LOX and CH₄ injection (chamber pressure and injection temperature respectively lower than critical pressure and temperature for both LOX and CH₄) ; one operating point: TH, has transcritical LOX and CH₄ injection (chamber pressure above LOX and CH₄ critical pressure and injection temperatures below LOX and CH₄ critical temperature), and one operating point: TL is characterized by a chamber pressure in between LOX and CH₄ critical pressures, and injection temperatures lower than LOX and CH₄ critical temperatures. For the injector without recess, only one operating point has been characterized, very similar to the TH operating point tested with the recessed injector, to enable comparison of both configurations at iso-operating conditions.

Operating conditions are presented in table 1 for the 4 selected experiments. Each operating condition corresponds to a time-averaged operating point calculated over a stabilized operating point time step. Typical duration for this time step is at least 10 s (cf. figure 3).

Table 1. Selection of 4 operating points for liquid/liquid (LL / LH) or double transcritical (TL / TH) conditions

Operating point ^a	LL	TL	LH	TH
LOX Mass flow (g/s)	20,6	19,3	21,8	36
CH ₄ mass flow (g/s)	59	65,2	85,2	147,1
MR	0,35	0,25	0,256	0,245
T LOX (K)	118	124	117	113
T CH ₄ (K)	143	142	145	144
P (bar)	27,4	50,1	32,7	55,7

^aTime-Averaged over stabilized operation time step

A typical temporal evolution of chamber pressure and mass flows is shown on figure 3 to illustrate stabilized operating conditions over the chosen time step.

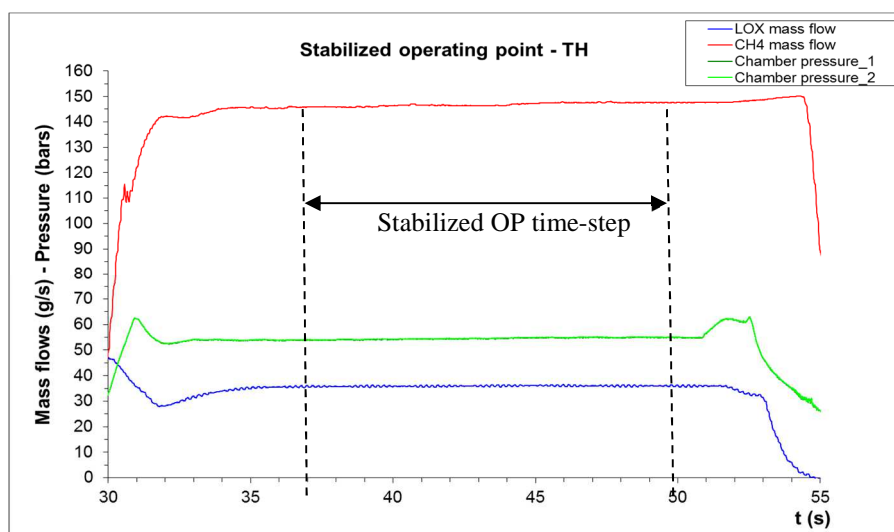


Figure 3 – Typical temporal evolution of mass flows and chamber pressure over stabilized operating point (TH) time step

2.3 Imaging and measurements set-up

2.3.1 Imaging set-up

Two main complementary imaging systems were set with a large field of view, in order to see the LOX and CH₄ jets and the flame locations synchronously (cf. figures 4 and 6).

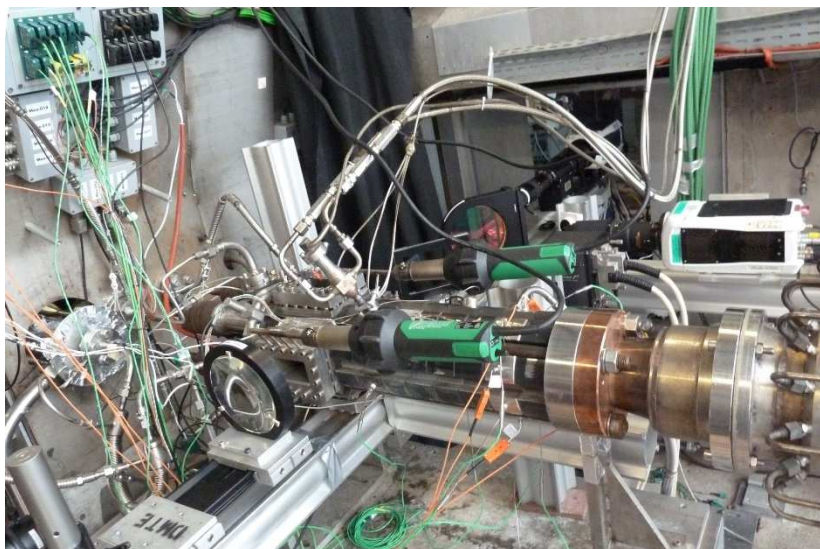


Figure 4. Optical diagnostics implemented on MASCOTTE test bench – Simultaneous high-speed OH* chemiluminescence and shadowgraphy

Shadowgraphy consists in taking pictures of the illuminated liquid jet by a light source located opposite to the camera (cf. Figure 6). In order to visualize the dynamics of the dense oxygen and methane jets at the injector exit, a high-speed v711 FAST camera from Vision Research was used. It is equipped with a CMOS sensor of 1280 x 800 pixels. This 12-bit monochrome camera records the signal on 4096 grey levels, with an active sensor size of 1280 x 720 pix² and a frame frequency set at maximum 7,4 kHz. The camera is equipped with the FAST option, enabling a minimum exposure time of 300 ns, which limits the natural flame emission. A 200 mm fixed focal length is set on the camera. A filter is mounted on the lens of the camera to select only the light from the backlight and remove remaining visible flame emission. The filter is centred around a 648 nm wavelength, with a maximum transmission of 80%, and a 12,5 nm full width at half maximum. The light source is a Cavilux Smart 400W pulsed laser source emitting in the red at 640 +/-10 nm. Minimum light source impulse duration is set to 50 ns maximum, enabling flow structure freezing.

Chemiluminescence imaging was operated simultaneously to visualize the flame reaction zone. The reaction mechanisms involved in combustion processes are numerous and complex. They consist of a large number of elementary reactions involving generally free radicals and molecules. In the combustion zone, elemental reactions produce radicals directly on excited energy levels. These species, that are out of thermodynamic equilibrium, relax spontaneously and almost instantaneously by emitting a photon characteristic of a transition energy to a lower level. This resulting light emission, which is characteristic of spontaneous radiative relaxation of species chemically created on excited states, such as the excited OH radical, denoted OH*, is called chemiluminescence. In the case of LOX/CH₄ cryogenic jet flames, few data are available in the literature. For example, Lux et al. [9] have studied the emission spectrum of high-pressure LOX/CH₄ flames. An intense emission peak observed around 310 nm is due to the presence of OH radical whereas another high intensity peak around 430 nm is due to another radical, CH. Both radicals are known to be produced by combustion in the chemical reaction zone. Other species, such as C₂, known to be a soot precursor, can be identified by several small peaks, called Swan bands. Depending on operating conditions considered, the continuous emission background, between 350 nm and 650 nm, which can be attributed to larger molecules such as CO₂, can be too intense to see the Swan bands, whereas OH and CH are generally intense enough to come out from the background and can thus be used as markers of the reaction zone for imaging purpose. This has been verified on LH operating point (cf. figure 5). Nevertheless, the relative intensity of the OH* peak being higher than the CH* one in our test conditions, OH* chemiluminescence seems an easier marker for reaction zones, with a better signal/noise ratio. Moreover, in a preliminary test campaign with similar operating conditions, OH* and CH* emission were

recorded simultaneously. Images analysis showed very similar flame topology, thus only one diagnostic – OH* emission - was finally implemented in the present campaign.

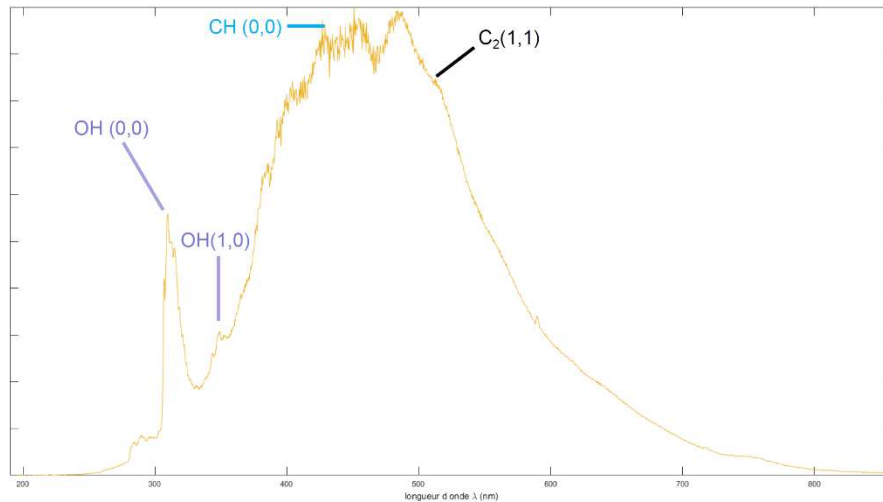


Figure 5. Emission spectrum of the LOX/CH4 flame at LH operating point

In order to visualize the reaction zone with OH* chemiluminescence, a UV imaging system was set up on MASCOTTE test bench (see Figure 6). It consists of an intensified high-speed camera (V711 32GB), with a CERCO 2085 UV lens adapted to ultraviolet light and a filter adapted to the spectral signature of the OH* radical. The focal length of the lens is fixed at 98 mm, with an aperture at its maximum: f/2.8 or at f/8. The OH* filter mounted on the UV lens has a maximum transmission of 70% at 310 nm and a 10 nm half-width. The gain of the intensifier was fixed at 600 V and the gate time of the intensifier was variable, depending on the flame studied, to obtain the best signal dynamics (between 2 and 5.2 μ s).

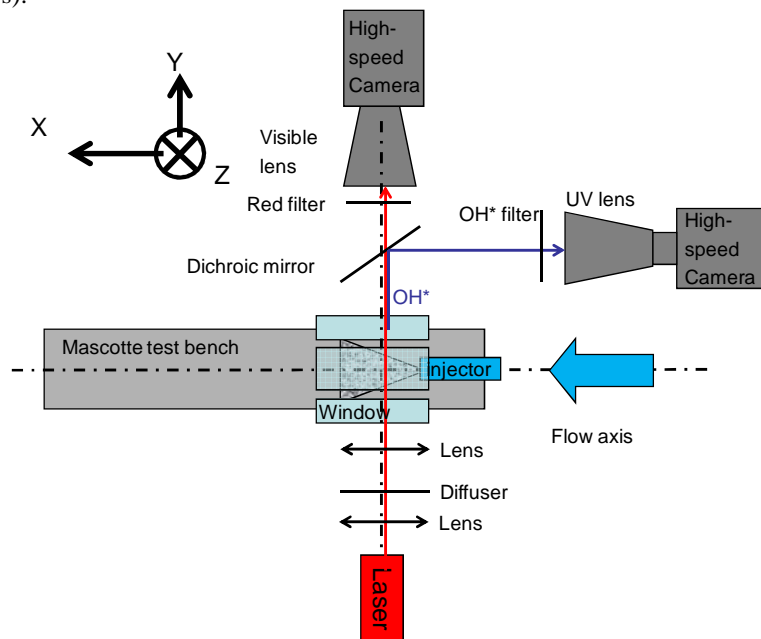


Figure 6: Imaging setup arrangement (top view) with shadowgraphy and chemiluminescence visualizations

OH* emission and shadowgraphy are focused on the same field-of-view, with the same spatial resolution, thanks to the use of a dichroic mirror that separates UV light coming from the OH* chemiluminescence towards the intensified camera and the visible light coming from the laser towards the high-speed camera used for shadowgraphy. Moreover both images are recorded at the same instant, at maximum 7400 frames/s, as the short laser pulse is emitted during the intensifier gate of the intensified camera. Thus both types of images can be directly superimposed as shown in the results section.

Finally, the flame emission spectrum, presented on figure 5 has been recorded in a range between 188 and 860 nm during one test day, using an Ocean Optics S2000 spectrometer, with a resolution of 0,37 nm. Flame emission is collected by a lens and an optical fiber placed in front of the BHP window, every 27 ms during 20 s maximum.

2.3.2 Other measurements set-up

A 8-thermocouples rake (4 of K type and 4 of S type) was located in the downstream part of the chamber, on the BHP chamber 7th module (cf. fig.1), in a section where the combustion is supposed to be complete and the combustion products homogeneous. Each thermocouple was inserted at a different radial position to check hot gases homogeneity in a section (cf. fig. 7).

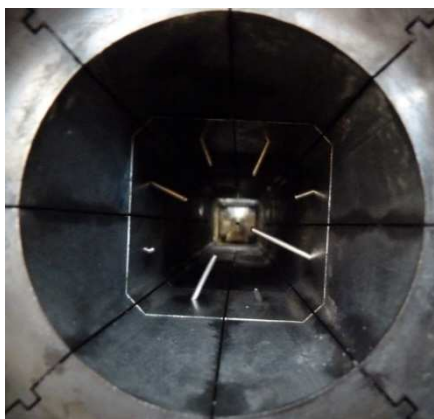


Figure 7 - Intrusive thermocouples positions in BHP chamber 7th module – Visualization from downstream

In addition, two local heat-flux transducers, based on surface temperature measurements (cf. [8]), have been implemented on the upper and lower wall of the optical module, in order to get a first estimation of wall heat losses. Several wall thermocouples have also been implemented at different depths inside the chamber wall or on the external walls along the chamber to monitor wall temperature evolution along the test.

Chamber pressure is measured by two Kulite sensors and by a Kistler sensor (dynamic pressure). LOX and CH₄ injection temperatures are measured downstream injection valves by a PT100 probe, and injection pressures are measured by Kulite and Kistler sensors (dynamic pressures) also downstream of injection valves. Dynamic pressure signals are acquired at a frequency of 20 kHz.

3. Experimental Results

3.1 OH* emission and shadowgraphy images analysis

3.1.1. Flame and dense jets topology

For all operating conditions tested, flame is visible right from the injector exit (cf. figure 8). It is not possible to say whether flame is really anchored to the injector lip due to the recess, but no intermittent flame detachment outside the recess has been observed in the high speed visualizations. Flames are always rather short, closed or almost closed in the window section, suggesting complete combustion very early in the chamber compared to the full chamber length.

For all operating points, OH* emission images in UV domain show two different features: a central brighter zone, featuring the flame, partially perturbed by a more diffuse emission zone, concentric to the first one (cf. figure 9). This more diffused emission seems to come from a dense phase or condensates, having a large-band emission range, because it has also been put in evidence in a previous campaign on CH* chemiluminescence images (visible domain), and because it is visible in the flame region and also outside the flame. From a radiative point of view, it could be classified as a grey body. Owing to the large amount of such dense phase present in the flow, it must contain at least one of the major gaseous species in the combustion products, i.e. CH₄, H₂, H₂O or CO₂ (results given by thermochemical calculation, COPELIA). From a thermodynamical point of view, the most probable candidate for condensation in all operating conditions tested is water: at 30 bar, it is sufficient to cool it down to 507 K to get it

liquid; and at 60 bar, 548 K is sufficient to get condensation. These temperatures values could be reached easily in particular in the recirculation zone, due to excess methane present in large quantities in this region and to the low methane injection temperature (cf. table 1). This will be verified in the numerical simulations section.

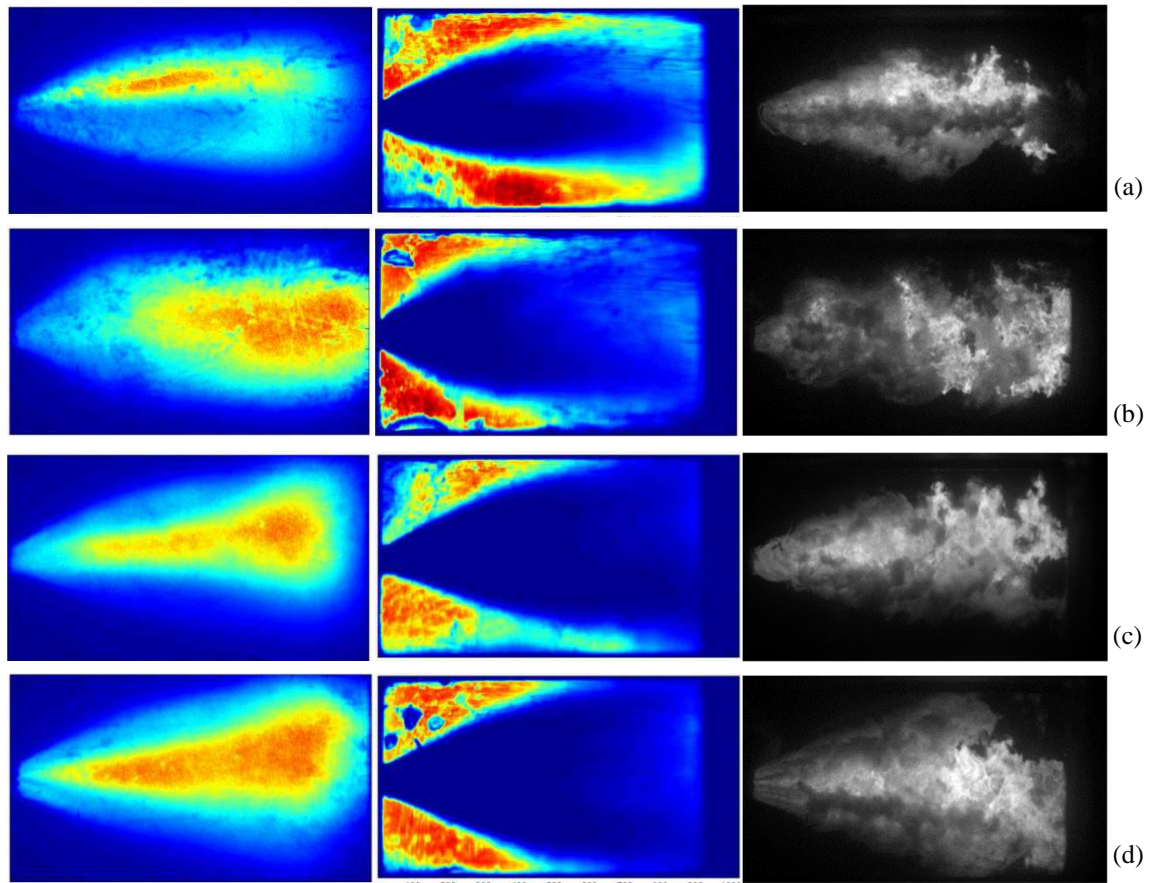


Figure 8. Time-averaged OH* emission (left), time-averaged shadowgraphs (center) and instantaneous OH* emission (right) for operating points LH (a), LL (b), TH (c), and TL (d).

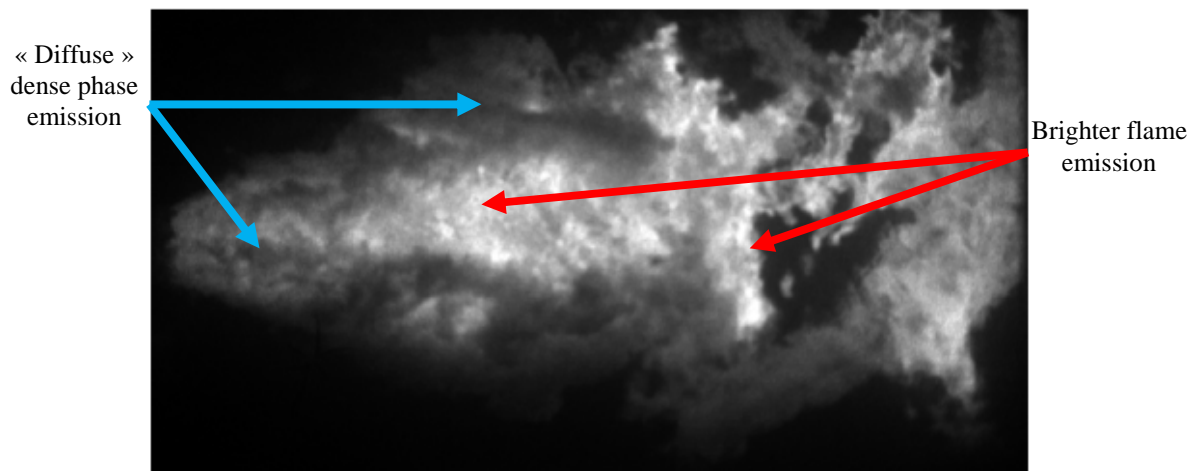


Figure 9. Evidence of “diffuse” dense phase emission around brighter flame emission – Instantaneous OH* emission image - TL operating point

Perturbation of the OH* emission signal by the diffuse fluid emission inhibits performance of Abel transforms on average OH* emission images, initially envisaged to better put in evidence the flame front topology and compare it to past studies [2]. Nevertheless one could argue that the presumed “double flame front” put in evidence in [2] in double-transcritical flames may be instead an evidence of the same “diffuse” fluid large band emission as shown in the present

studies. The inner brighter zone on OH* emission images from our tests is comparable to the inner zone of T1 flame put in evidence in [2]. Further characterizations will be needed in the future to try to identify the nature of the dense phase responsible for large band emission.

Soot or at least “soot-like” deposits are found on BHP windows after each test. Deposit seems progressive along test duration, not occurring only during transients. These solid particles may be also part of the “diffuse “dense phase observed on OH* emission images. Liquid fluid (water ?) is also streaming across windows and recirculating in the first half of the visualised zone. Finally, ice formation can be put in evidence by a dense zone, corresponding presumably to a ring, at the exit of the injector, at least for all operating conditions with injector recess. The ice ring growth occur up to a few millimeters length before disappearing and reappearing again (cf. figure 10, dark zone at injector exit on OH* emission images). This evidences again the very cold environment in the recirculation zone immediately downstream the injector, prone to water condensation and even icing. The ice ring diameter is correlated to the external frontier of diffuse dense phase emission on OH* emission images.

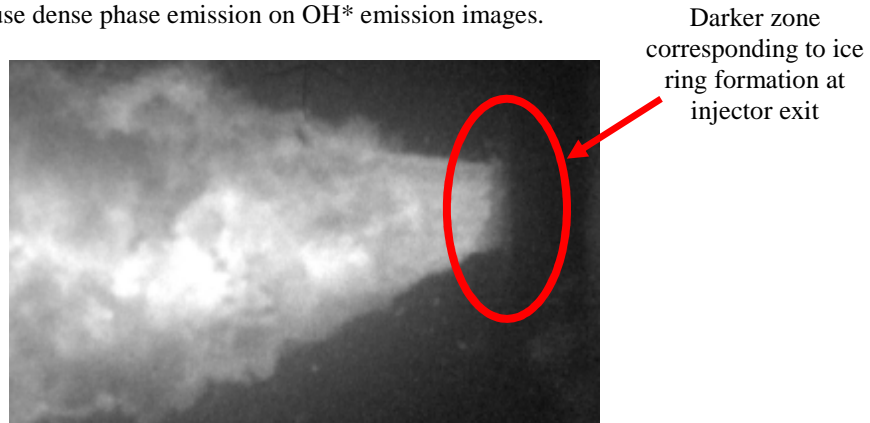


Figure 10. Evidence on ice ring formation at injector exit for operating point TH – Instantaneous OH* emission.

3.1.2. Comparison between recessed and non-recessed injectors

As for recessed injector, non-recessed injector evidences flame presence right at the injector exit, clearly showing in this case an anchored flame directly at the injector exit. Differences can also be observed between OH* emission and shadowgraphy images of both configurations (cf. figure 11):

- OH* signal is more intense in the first half of window and flame seems shorter in the recessed configuration compared to the non-recessed configuration,
- “3 branches” shadowgraphy images for the non-recessed configuration suggests that the LOX jet, featured by the central branch”, is longer than in the recessed configuration.

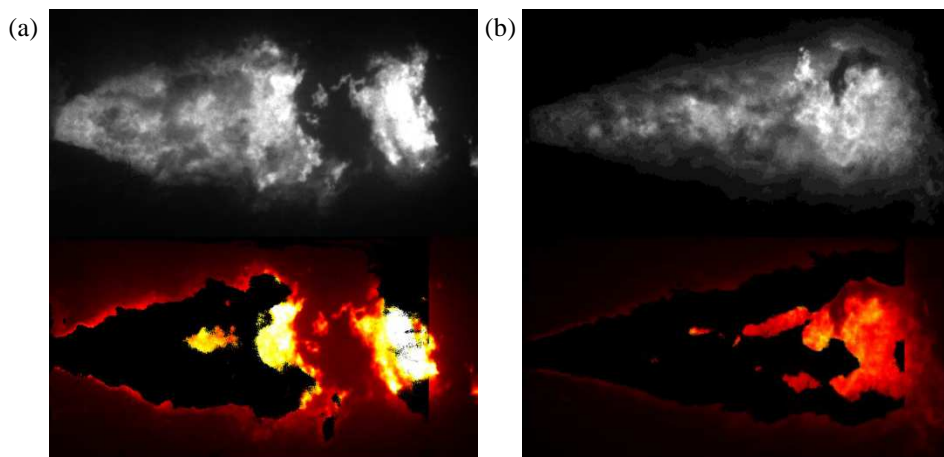


Figure 11. Instantaneous OH* emission in grey levels scale (up) and superposed instantaneous OH* emission and binarized shadowgraphs (down) for recessed injector (a) and non-recessed injector (b) @ TH operating point.

3.2 Combustion efficiency

Combustion efficiency η_{C^*} has first been evaluated for 4 operating points for the recessed injector plus for the injector configuration without recess under two main hypotheses:

- throat discharge coefficient is equal to one (verified by cold flow tests in a previous test campaign)
- wall heat losses are negligible.

It has been evaluated by comparison between the measured characteristic velocity C^* and the theoretical characteristic velocity C^*_{th} calculated using a ONERA/CNES in-house thermochemical code (COPELIA), developed by ONERA. COPELIA uses as input data time-averaged values of measured LOX and CH₄ mass flows and injection temperatures, and chamber pressure. Results produced by COPELIA have also been compared to CEA2 code [10] results for similar operating conditions, and show very comparable results (less than 1% difference on calculated adiabatic hot gases temperature). COPELIA or CEA2 offer the possibility to take into account or not the formation of solid carbon C(s) within combustion products. At equilibrium, C(s) mass fraction gets up to 10 % or more depending on considered operating point. This seems rather high compared to the small deposit found on BHP windows after each test, suggesting that equilibrium is not fully reached in the experiment. When taking into account C(s), calculated adiabatic temperature gets lower, but only in a very limited extent, less than 20 K.

Table 2. Evaluation of combustion efficiencies for selected operating points

Operating point ^a	LL	TL	LH	TH	TH w/o recess
LOX Mass flow (g/s)	20,6	19,3	21,8	36	35,8
CH ₄ mass flow (g/s)	59	65,2	85,2	147,1	145,8
MR	0,35	0,296	0,256	0,245	0,246
T LOX (K)	118	124	117	113	115
T CH ₄ (K)	143	142	145	144	148
P (bar)	27,4	50,1	32,7	55,7	54,8
η_{C^*}	0,906	0,888	0,859	0,861	0,852
T _{ad th} (K)	926	897	833	833	836
T _{meas. moy} (K)	732	656	607	609	602

^aTime-Averaged over stabilized operation time step

Overall, η_{C^*} values are rather low, despite obviously complete combustion evidenced by short flames shown by OH* emission images and homogeneous combustion products temperature profiles (apart from wall effects) measured downstream of the flame. Thus, at first sight, wall heat losses seem to be a good candidate to explain low calculated values for combustion efficiencies. In order to investigate this hypothesis, an order of magnitude estimation of average hot gases temperature loss due to wall heat losses has been made on operating point TH, using the locally measured surface wall heat flux ϕ (in the visualization section) and assuming it constant along the chamber. This hypothesis is judged relevant for order of magnitude estimation by analysis of intrusive fluid temperature situated at 0,5 mm from the wall in the visualization section, only few tens of K higher than intrusive fluid temperature at 2 mm from the wall in the last test section, compatible with limited and progressive cooling along the chamber walls after visualization section. From a global energetic point of view, heat losses can be written as:

$$\phi = \varphi \cdot S = C p_{hot\ gases} (T_{ad\ th} - T_{hot\ gases})$$

The hot gases heat capacity $C p_{hot\ gases}$ has been estimated by using the hot gases composition calculated by COPELIA for operating point TH. With this estimation, the calculated average hot gases temperature $T_{hot\ gases}$ taking into account

wall heat losses is decreased by about 20 K compared to the adiabatic theoretical value $T_{ad th}$, which is much lower than the actual measured temperature deficit (about 220 K for TH, cf. table 2). Of course, this analysis should be refined in the future, for example by enriching the test database with more heat flux measurements at different axial positions along the chamber. But it suggests anyway that other causes should be searched for explaining observed low combustion efficiencies:

- impact of possible H₂O condensation in recirculation zone and then vaporization downstream on local composition and possible displacement of global equilibrium;
- equilibrium not reached due to residence time too low for some elementary reactions and/or particular behavior of kinetics at very low mixture ratio (for e.g. intermediate products from intermediate endothermic reactions “frozen” due to too low temperature);
- Other ? ...

Despite reduced size of database, decrease of combustion efficiency with decreasing MR (see figure 12) can be shown as in other research studies (e.g. Tamura et al. [3], Soller et al. [6]) suggesting again possible non equilibrium effects (compatible with low temperatures) at very low mixture ratios.

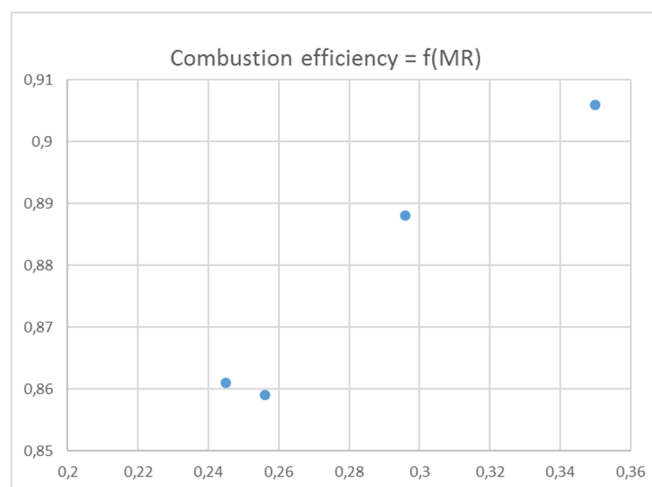


Figure 12. Increase of η_{c^*} with MR

It is also worth noting that η_{c^*} for the recessed injector configuration is about 1% higher than the non-recessed injector η_{c^*} confirming a slightly better performance of the recessed injector, coherent with slightly higher flame length and more intense OH* emission in the near injector region (see §3.1.2).

4. Numerical Simulations

4.1. CPS-C code and models presentation

The CFD code used for the computational analysis is an in-house code called CPS-C developed by CT Ingénierie (previously part of Bertin Technologies) in collaboration with CNES (cf. [12]). This code solves the Navier-Stokes equations in conjunction with the continuity, energy, turbulence and species equations. The numerical procedure is based on a second order (in space) approximate Riemann solver that allows evaluation of spatial fluxes at cell faces whereas second order-accuracy in time is achieved by a two-step explicit scheme. The main physical models used in these computations are the following:

- Real gas law (Redlich Kong Soave), and variable thermodynamic properties to represent the multi-species gaseous or real gas mixtures;
- The effects of turbulence are modelled with a k-epsilon model;
- The combustion process is modelled by an Arrhenius multi-reactions model, together with a specific LOX/CH₄ reduced kinetic scheme presented in §4.2.1 ;
- heat transfer at the walls can be calculated by using in-house CPS-C “thick layer“ wall law for boundary layers

4.2 Preliminary reduced kinetic scheme evaluation

Based on preliminary studies, a reduced LOX/CH₄ kinetic scheme, including 9 species and 21 reactions (denoted CH₄-O₂-21r-V3), has been built, based on :

- Dryer [11] kinetic scheme for methane combustion
- Eklund [13] kinetic scheme for H₂/O₂ combustion
- $\text{CO} + \text{O}_2 \leftrightarrow \text{CO}_2$ equilibrium reaction
- Water gas shift reaction (WGSR): $\text{CO} + \text{H}_2\text{O} \leftrightarrow \text{CO}_2 + \text{H}_2$
- $\text{CH}_4 + \text{H}_2\text{O} \leftrightarrow \text{CO} + 3\text{H}_2$ reaction present in Jones & Lindstedt [14] kinetic scheme, important for fuel rich methane combustion.

When building this simplified kinetic scheme, the objective is to be able to finally calculate with sufficient accuracy LOX/CH₄ combustion at moderate to high pressures (typically 20 to 100 bar), at both stoichiometric (MR_{st} = 4) or near stoichiometric mixture ratio (representative for flame front or hot gas flow in rocket engine main combustion chamber application) and very low mixture ratio (representative for hot gases in gas generator application, typically MR < 0,5).

4.2.1. Elementary calculations

In order to evaluate this newly built reduced scheme CH₄-O₂-21r-V3, comparisons are made in the following paragraph with several other schemes available from literature :

- Gri-Mech 3.0 [16] very detailed scheme, often used as reference in LOX/CH₄ modelling despite development and validation only for low pressures (up to 10bars) and air/CH₄ combustion
- a semi-detailed mechanism developed by DLR [5] for methane oxy-combustion at high pressure (called ReducedSens), including 23 species and 51 reactions derived from a detailed alkane oxidation mechanism dedicated to high pressures (called Full Mechanism) developed by Zhukov, including 207 species and 1260 reactions [17].

Kinetic schemes have been compared on main parameters characterizing chemical processes involving kinetics :

- Autoignition delay
- Counter-diffusion flame velocity
- Adiabatic flame temperature compared to theoretical chemical equilibrium.

Calculations have been performed with CANTERA code [18].

Autoignition delay

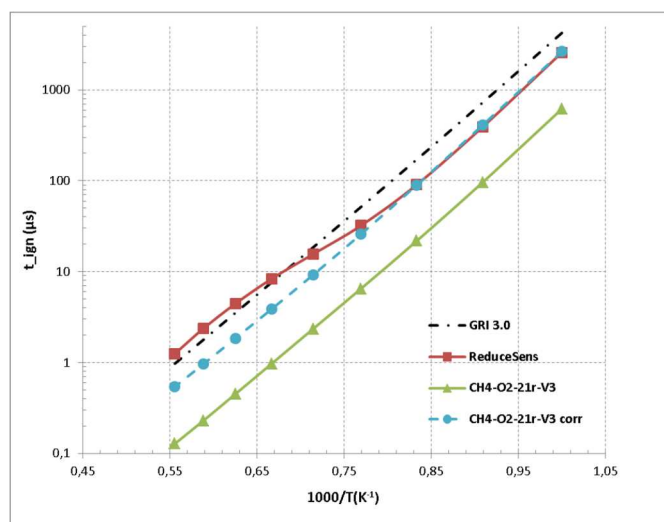


Figure 13. Autoignition delays in a stoichiometric LOX/CH₄ mixture at 60 bars for different kinetic schemes as a function of initial mixture temperature.

Autoignition delay has been evaluated for a stoichiometric LOX/CH₄ mixture at a pressure of 60 bar, as a function of initial temperature T (cf. figure 13). CH₄-O₂-21r-V3 underestimates ignition delay of a factor 4 at low temperatures and by a factor of 10 at high temperatures. Following this first evaluation, methane oxidation reaction into CO and

H₂O has thus been decelerated to be more representative for autoignition delays at low temperatures. The resulting corrected kinetic scheme is CH₄-O₂-21r-V3corr ; emphasis is put on the scheme precision on the low temperature side because ignition delays are so low at higher temperature that chemistry can be considered as infinitely fast in flame stoichiometric zones.

Counter-diffusion flame

Counter-diffusion flame test-case is taken from [5]. Again, CH₄-O₂-21r-V3 mechanism shows very good results compared to more detailed mechanisms. Comparison of temperature axial profiles through counter diffusion flame are shown on figure 14. Axial profiles of molar fraction for main species show also very good agreement. Main difference concerns a slight overestimation of OH peak by about 10% in the flame for CH₄-O₂-21r-V3 compared to ReduceSens. It has also been verified that results obtained with CH₄-O₂-21r-V3corr mechanism show only very limited degradation compared to CH₄-O₂-21r-V3 (+15K only on temperature peak value in figure 14 (a)).

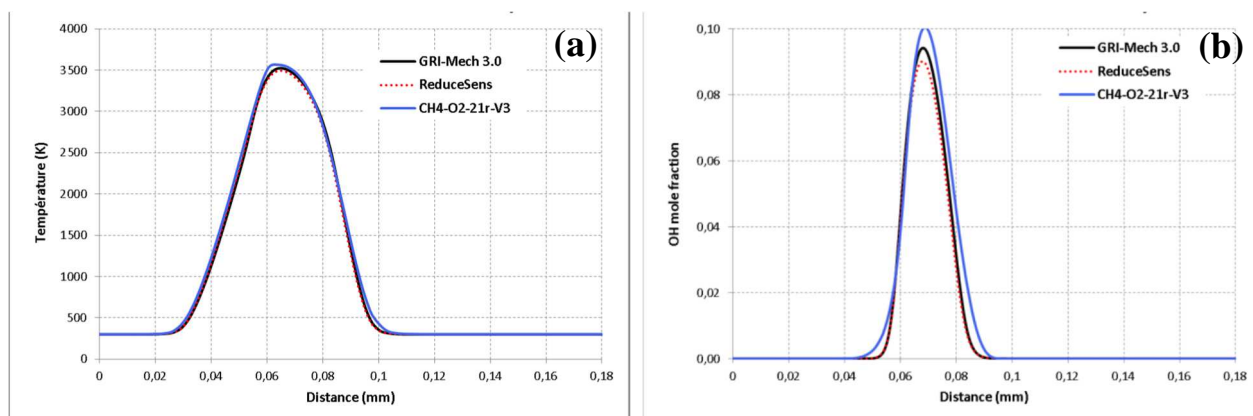


Figure 14 : Axial temperature profiles (a) and OH molar fraction profile (b) through the counter-diffusion flame for different kinetic schemes

Perfectly stirred reactor (PSR) calculations

PSR calculation is made for operating conditions corresponding to T1 operating point from [2]. Operation of the PSR is realized for a duration at least 10 times higher than the propellants residence time in the reactor. A constant pressure corresponding to T1 operating point is imposed in all PSR components. Such a calculation is made for GriMech3.0, ReduceSens and CH₄-O₂-21r-V3 mechanisms. Composition and temperature at convergence are then compared to thermodynamic equilibrium calculated with CANTERA without solid carbon production. CH₄-O₂-21r-V3 is able to retrieve both temperature and composition with a good precision for high pressure / low mixture ratio T1-type test case, better than the 2 other mechanisms.

Table 3 – PSR LOX/CH₄ T1 test-case results with 3 kinetic mechanisms compared to equilibrium calculations

	Equilibrium (CANTERA w/o C _(s))	GriMech3.0	ReduceSens	CH ₄ -O ₂ -21r-V3
T(K)	953,1	1030,2	1014,9	959,2
P(bar)	54	54	54	54
Y _{CH₄}	0,679344	0,680882	0,653773	0,681627
Y _{CO}	0,095246	0,058790	0,057364	0,091705
Y _{CO₂}	0,131641	0,062541	0,070113	0,131764
Y _{H₂O}	0,076567	0,149464	0,14294	0,078406

4.2.2. Application to G2 and T1 flame ([2])

2 test-cases selected from [2] have been preliminary calculated using CPS-C to validate the chosen modelling strategy to be applied on test-cases defined from the recent test campaign results : test-case G2 (transcritical LOX and gaseous

methane injection) and test-case T1 (transcritical LOX and CH₄ injection). T1 operating conditions are very similar to TH operating conditions. Calculated temperature maps are presented on figure 15, and compared to OH emission from [2]. For G2, the overall “mushroom”-type flame topology, due to a large recirculation zone downstream of the flame (cf. [15]), is well retrieved, as well as the flame length. For T1, a longer flame length compared to G2 is observed as shown by tests, but no external second flame front could be put in evidence in the calculations. This will have to be further analysed at the light of dense phase diffuse emission around the flame put in evidence during our recent campaign (cf. §3). The inner reactive front topology is also well captured despite too low flame brush angle in the first part of the calculated flame compared to experimental flame.

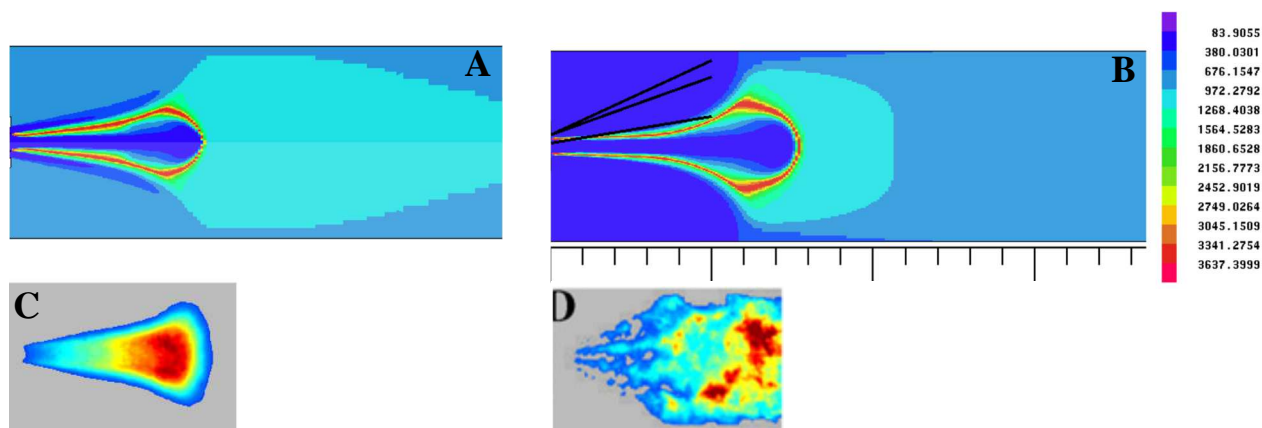


Figure 15. Calculated temperature map (A) G2 operating point (B) T1 operating point (2D calculations) – average OH* emission for G2 operating point (C)* instantaneous OH* emission for T1 operating point (D)* (extracted from [2]).

Additional post-processing of T1 calculations results have been made to assess the water condensation plausibility in the recirculation zone downstream of the injection plane (cf. figure 16). It is shown that the H₂O mass fraction in this zone is not negligible (around 4%) with temperatures lower than the local saturation temperature. A further step would be the modelling of condensation phenomenon to account for possible impacts on local composition and thermal stratification downstream.

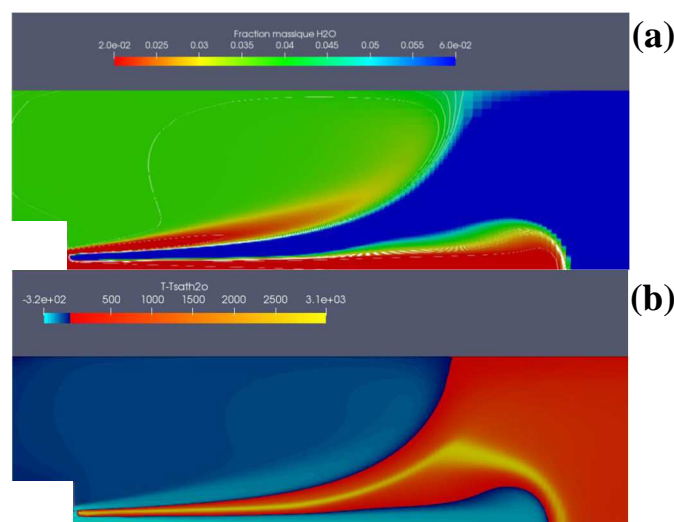


Figure 16. Calculated H₂O mass fraction (a) map of delta-temperature to H₂O local saturation temperature (b) in the near injection region for T1 operating point (2D calculations)

3D calculations of the T1 flame have also been performed, showing that the calculated flame topology and length is only marginally different from 2D calculated flame (see figure 17). This ensures the validity of possible parametric studies to be performed on the basis of 2D calculations.

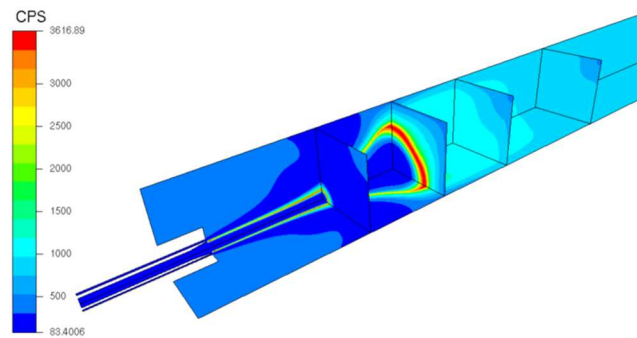


Figure 17. Calculated temperature map for T1 operating point (3D calculation)

4.2 Calculation of TH operating point for recessed injector

The modelling methodology presented above has been applied to one test-case selected from § 3: operating point TH. For numerical test-case definition, operating point TH presented in table 1 have been redefined using test data time-averaged over the time step exactly corresponding to visualizations acquisition time step (about 3 s duration). Preliminary 2D calculations have been realized on this test-case. First results are shown on figure 18.

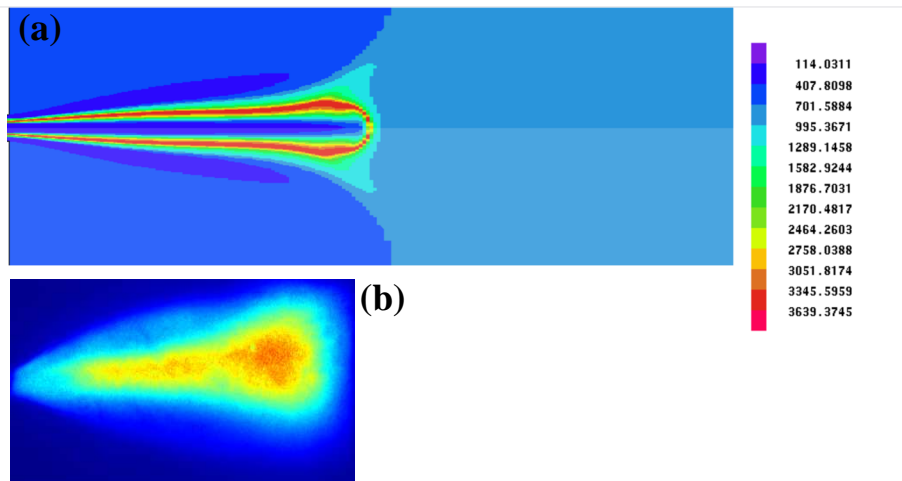


Figure 18. Temperature map for TH operating point – 2D calculation (a) – averaged OH* emission (b)

Flame features a topology similar to T1 flame calculated in §4.2.2, with lower opening angle and slightly longer flame. Compared to measured OH* emission averaged map, the flame topology seems reasonably captured, with slight underestimation of opening angle and slight overestimation of flame length. This should be confirmed with 3D calculations. Wall heat losses are taken into account in this calculation (see §4.1). A wall temperature is imposed on BHP lateral walls as well as on the injection plane, equal to the temperature measured on visualization module lower walls. In injectors, a wall temperature equal to the LOX or CH₄ injection temperature is imposed. In the downstream thermocouples measurement plane, average calculated temperature is 809 K, for an average measured value of 608 K, and a theoretical thermochemical equilibrium temperature calculated by COPELIA respectively equal to 841 K or 857 K with production of solid carbon or without. The current modelling, taking into account heat losses at the wall is thus not sufficient to retrieve the temperature deficit to equilibrium value shown by measurements. One could even argue that due to the over-estimation of hot gases temperature in the calculation, the calculated wall heat losses are even still over-estimated when using an imposed wall temperature from measurements as boundary condition. This is partially validated by comparison between the locally measured heat flux value on the visualization module walls, and the calculated one: locally calculated heat flux has the right order of magnitude but is about 30% higher than the measured one.

5. Conclusions and perspectives

CNES, ONERA and CT Ingénierie have held R&D activities dedicated to the characterization of cryogenic LOX/CH₄ combustion in rocket engine gas generators conditions, at low mixture ratio and with both propellants injected in

transcritical or liquid conditions. Several reactive coaxial mono-injector test-cases, including flame visualizations, have been built at ONERA MASCOTTE test bench, all characterized by measured hot gas temperatures lower than theoretical chemical equilibrium temperature. Flame topology has been compared to past results in similar operating conditions, which had shown a typical “double flame front” for double transcritical flames. This particular feature has not been retrieved in new tests, instead the flame OH* emission is shown to be perturbed by a dense phase emitting in a large wavelength band, supposedly condensed water or condensed water mixed with soot or soot precursors.

Numerical simulations have been set up to study possible cause(s) for this temperature deficit, using a reduced kinetic scheme adapted to low mixture ratio and high pressure LOX/CH₄ combustion. Flame topologies are rather well retrieved by simulations. Impact of wall heat losses on hot gases has been studied and has shown that the temperature deficit is only very partially explained by wall heat losses. Calculations have shown that water condensation is possible in the recirculation downstream of the injection plane. This supports hypothesis of condensed water as possible contributor to the diffuse dense phase emission seen on OH* emission images. Impact of such phenomenon on downstream stratification and on local composition needs to be further assessed. Further steps are needed, both on experimental and numerical side, to prove some hypotheses formulated in this study and to better understand particular features encountered in LOX/CH₄ flames at low mixture ratio.

Acknowledgments

The authors would like to thank the members of the MASCOTTE test bench and optical diagnostics teams for their involvement during the preparation and conduction of the experimental test campaign. This work is supported by CNES Launchers Directorate Liquid Propulsion R&D program.

References

- [1] Vingert et al., A rocket under a magnifying glass, Challenges in Combustion for Aerospace Propulsion, *Journal of Aerospace Lab*, Issue 11, June 2016
- [2] Singla et al., Transcritical oxygen/transcritical or supercritical methane combustion, *Proceedings of the Combustion Institute* v.30, pp. 2921–2928, 2005
- [3] Huebner et al., High pressure LOX/hydrocarbon preburners and gas generators, *NASA CR-161342*, 1981
- [4] Tamura et al., LOX methane staged combustion rocket combustor investigation, *AIAA 87-1856*, 1987
- [5] Zhukov et al., A compact reaction mechanism of methane oxidation at high pressures, *Progress in Reaction Kinetics and Mechanism*, Vol. 43(1), pp. 62-78, 2018.
- [6] Soller et al., Characterization of a LOX/LCH₄ gas generator, *Space propulsion conference, Cologne*, 2014
- [7] Vingert et al., Experimental investigations of liquid oxygen/methane combustion at low mixture ratio at the MASCOTTE test facility, *ISTS conference*, 2019
- [8] Guernigou et al., Mise au point de fluxmètres à température superficielle, *La Recherche Aéronautique* n°1980-3, pp. 159-168, 1980
- [9] Lux et al., Flame Stabilization in High-Pressure Liquid Oxygen/Methane Rocket Engine Combustion, *Journal of Propulsion and Power*, Vol.25, Issue 1 pp.15-23, 2009
- [10] McBride et al., Chemical Equilibrium Applications – NASA Glenn Chemical Equilibrium Program CEA2, May 21, 2004, available at : www.grc.nasa.gov/www/CEAWeb/ceaRequestForm.htm
- [11] Dryer, High Temperature Oxidation of CO and CH₄ in a Turbulent Flow Reactor, Rep. AMS 1034-T. *Ph.D. Thesis, Aerospace and Mechanical Sciences Department, Princeton University, Princeton, New Jersey*, 1972.
- [12] Prediction and analysis of combustion instabilities in a model rocket engine, *Journal of Propulsion and Power* v. 30(4), pp.978-990, July 2014
- [13] Eklund et al., Calculation of supersonic turbulent reacting coaxial jets, *AIAA Journal* v.28 n°9, Sept. 1990
- [14] Jones et al., Global reaction schemes for hydrocarbon combustion, *Combustion and Flame* v.73, n°3, pp.233-249, 1988
- [15] Schmitt et al., Large-Eddy Simulation of oxygen/methane flames under transcritical conditions, *Proceedings of the Combustion Institute* v.33, issue 1, pp.1383-1390, 2011
- [16] Smith et al., GRiMech 3.0, available at : www.me.berkeley.edu/gri_mech/
- [17] Zhukov et al., Development of a skeletal kinetic mechanism of methane oxidation for higher pressures and temperatures, *Space propulsion conference, Roma*, 2016
- [18] Goodwin et al., CANTERA : an object oriented software toolkit for chemical kinetics, Thermodynamic and Transport Processes, V2.3.0, 2017, available at www.cantera.org